Resonant response and optimal energy harvesting of an elastically mounted pitching and heaving hydrofoil

Yunxing Su* and Kenneth Breuer
School of Engineering, Brown University, Providence, Rhode Island 02912, USA

(Received 19 February 2019; published 20 June 2019)

The aeroelastic response and energy harvesting performance of an elastically mounted hydrofoil subject to a prescribed pitching motion are experimentally studied using a cyber-physical force-feedback control system in a uniform flow. By taking advantage of this cyber-physical system, we systematically sweep through the parameter space of the elastic support (stiffness, damping, and mass) for various frequencies of the prescribed pitching motion. It is found that the flow-induced heave amplitude and the energy harvesting performance are both strongly affected by the frequency ratio between the prescribed pitching frequency and the natural frequency of the system and the damping coefficient. In particular, for a fixed damping coefficient, the maximum flow-induced heave amplitude is achieved at the resonant condition (frequency ratio of 1), which also gives rise to the highest energy harvesting performance. At this resonance condition, though a smaller damping produces a larger heave amplitude, the optimal energy harvesting performance is obtained consistently at an intermediate damping coefficient of 1.5. In addition, at the resonance condition, the heave amplitude, or Strouhal number, and the hydrodynamic forces on the foil are both found to collapse well for different reduced frequencies, suggesting a similarity in the vortex dynamics generated by the elastically mounted system. A low-order model based on classical vibration theory is formulated to reproduce the power coefficient using the damping coefficient and Strouhal number, and we find that the power coefficient predicted by the model agrees well with that measured in the experiment over the range of reduced frequency explored.

DOI: 10.1103/PhysRevFluids.4.064701

I. INTRODUCTION

Hydrokinetic energy is gaining importance these years as it is clean and renewable compared to the conventional fossil fuels and also due to its large amount of resources available in the oceans and rivers. Instead of the widely used conventional rotatory turbines, oscillating hydrofoils are reported to offer an alternative solution to extracting the hydrokinetic energy owing to its high efficiency, shallow water feasibility, and aquatic life friendliness [1]. Thus far, most of the studies of oscillating foils in literature have focused on investigating the energy harvesting performance with prescribed foil kinematics. Hydrofoils in these studies are driven through prescribed trajectories and then the forces and moment of torques are measured to calculate the power extracted by the system. A wide-spread parameter space has been explored to optimize the power extraction performance by a sinusoidal heaving and pitching foil, including the pitch and heave amplitudes, reduced frequency, phase difference between pitching and heaving motions, pitching axis location, aspect ratio, and the geometry of the leading edge [2,3]. Particularly, researchers [2,4] numerically conducted a parametric sweep over the motion frequency and the pitch amplitude and reported

*Yunxing_Su@brown.edu

an optimal efficiency of 0.34 at a reduced frequency of 0.15, pitch amplitude of 75°, and heave amplitude of one chord length. As discussed by the authors, the lift force and the synchronization between the force and the corresponding velocity play primary roles in the energy extraction performance. A phase difference of 90° between the heaving and the pitching motions was shown [1,4] to produce the maximum power extraction output owing to the optimal force-velocity synchronization.

The lift force on an oscillating hydrofoil can be decomposed into two components: the noncirculatory component from the inertial reaction of the fluid, which is closely related to the foil's acceleration; and the circulatory component associated with the vortex dynamics on the foil [5–8]. The formation and evolution of leading edge vortex (LEV) on the hydrofoil have been shown to be critical in the lift force generation [9], the force-velocity synchronization, and the power extraction [2]. Kinsey and Dumas [2] also reported that simulations with the same frequency and effective angle of attack (AOA) generated similar flow characteristics (LEV formation), resulting in similar lift force histories. By varying the reduced frequency and Strouhal number while keeping the same effective AOA of an oscillating foil, Baik *et al.* [10], with the help of flow field measurements, confirmed the importance of effective AOA and reduced frequency in determining the LEV evolution and the forces exerted on the foil.

Studies [11–15] showed that nonsinusoidal motion profiles were potentially beneficial to the power extraction performance of a flapping hydrofoil. Specifically, Xiao *et al.* [16] investigated the effects of trapezoidal pitch profiles on the energy harvesting performance with a fixed sinusoidal heaving motion. The researchers reported that the heave component of power extraction increased with the trapezoidal profiles while the pitch component demonstrated otherwise. With the help of particle image velocimetry (PIV) measurements, Rival *et al.* [17] examined the leading-edge vortex evolution for different motion profiles and reported that the lifetime of the LEV on a heaving airfoil could be noticeably extended with a delayed vortex growth and pinch-off by fine tuning the foil kinematics. By examining the LEV formation on a pitching and heaving hydrofoil with nonsinusoidal kinematics, Fenercioglu *et al.* [18] reported that a larger rotation speed at the pitch reversal led to an earlier vortex shedding but with a higher strength. For energy harvesting of an oscillating hydrofoil with trapezoidal pitch profiles, Deng *et al.* [19] and Teng *et al.* [15] pointed out that the large effective AOA maintained through most of the cycle was essential in increasing the power extraction performance.

Recently, a novel design of the oscillating energy harvester is introduced and examined with a prescribed pitch motion and a flow-induced heave motion, which is usually referred as semipassive energy harvester [20–24]. In those systems, the passivity of the heave motion is achieved by either numerical simulations or physical springs and dampers. The heave motion response and the energy harvesting performance of the energy harvesters are determined by the stiffness, damping, and mass of the passive heave system. However, the parametric volumes (stiffness, damping, and mass) of these semipassive energy harvesters are limited due to the difficulty in changing the values of the physical springs and dampers. One alternative solution to avoiding such limitations is by using a cyber-physical system, in which a force-feedback control system provides an easy access to varying the system parameters (stiffness, mass, and damping). Initialized by Hover *et al.* [25] for the investigation of marine cables, the cyber-physical system was then demonstrated in the studies of vortex-induced vibration of a circular cylinder [26–29] and the dynamics of the leading edge vortex on a flat plate [30–32].

In the current study, a force-feedback cyber-physical system is used to achieve the passive or elastically mounted heave motion, while the pitch motion is prescribed by the user. We focus on optimizing the energy harvesting performance of an elastically mounted hydrofoil via a parametric sweep across the elastic parameters (stiffness, damping, and virtual mass). Then follows the analysis on the elastic parameters effects on the response of the elastically mounted system. In addition, the nonsinusoidal pitch profile effects on energy extraction are also investigated to capture the optimal pitch kinematics for energy harvesting.

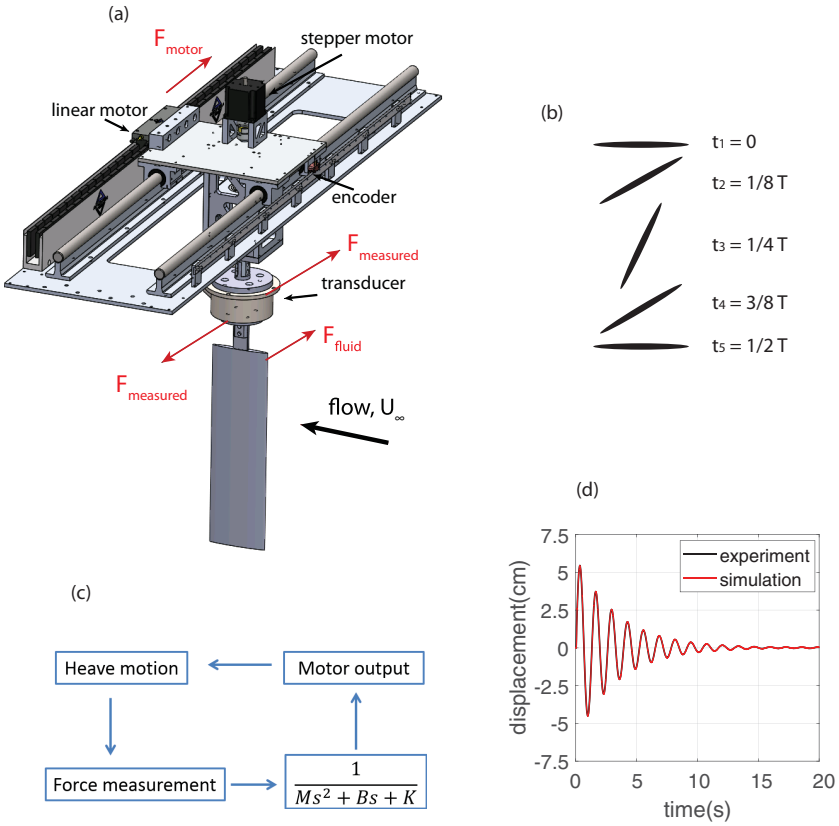

FIG. 1. (a) Experimental system with the hydrofoil, force transducer, rotary and linear motors and encoders; (b) top view of one typical kinematics of the hydrofoil ($\pi/2$ phase difference between pitch and heave) with five different positions (only the downstroke is shown here due to its stroke symmetry); (c) the force-feedback control system diagram; (d) "ring-down" experiment comparing the measured heaving position and the theoretical position.

II. EXPERIMENTAL SETUP

A. Physical apparatus

The experiments were carried out in a free-surface circulating flume at Brown University with a test section of 80 cm (wide) × 60 cm (deep) × 4 m (long). Experiments were typically conducted at a free-stream velocity, U_∞, of 0.4 m/s, measured using an Acoustic Doppler Velocimeter (Vectrino, Nortek AS), positioned upstream of the experiment area. As shown in Fig. 1(a), the hydrofoil has an elliptical profile with chord length, $c = 0.1$ m, and span, $s = 0.35$ m (aspect ratio, AR $= 3.5$). The foil is vertically suspended from a six-axis force-torque sensor (ATI IP65), which is attached to a shaft controlled by a rotary motor for pitch motion (Applied Motion Products HT23-593D) and linear motor (Aerotech BLM-142-A-AC-H-S-5000) for transverse heave motion across the flume. In these experiments, the pitching kinematics of the hydrofoil are prescribed by the user. However, in the heave direction, the hydrofoil is free to move, subject to fluid and inertial forces, and connected to a virtual spring-damper that is defined using the cyber-physical control system. Figure 1(b) demonstrates one of the typical hydrofoil motions, in this case with a phase difference of $\pi/2$ between the pitching and heaving motions. Five different hydrofoil positions are marked at different times during the downstroke of the cycle. The instantaneous heaving position, $h(t)$, and pitching position, $\theta(t)$, were measured in real time using optical encoders (U.S.

Digital E3-2500-250-IE-D-D-1) and the heaving position also served as the feedback signal for the servo motor controller. The forces (lift and torque) on the hydrofoil were directly measured by a six-axis force-torque sensor and sampled at 2000 Hz using an analog-to-digital converter (National Instruments). The nondimensional lift and torque coefficients are defined as

$$C_L = \frac{F}{0.5\rho U_\infty^2 sc} \quad \text{and} \quad C_\tau = \frac{\tau}{0.5\rho U_\infty^2 sc^2}. \tag{1}$$

As discussed in Refs. [2,3], the power extraction can be divided into contributions from the heave component and the pitch component. The cycle-averaged power coefficient and energy harvesting efficiency are then given as

$$\text{heave power:} \quad C_h = \frac{< F(t)\dot{h}(t) >}{0.5\rho U_\infty^3 cs}, \quad \text{pitch power:} \quad C_p = \frac{< \tau(t)\dot{\theta}(t) >}{0.5\rho U_\infty^3 cs}, \tag{2}$$

$$\text{heave efficiency:} \quad \eta_h = \frac{< F(t)\dot{h}(t) >}{0.5\rho U_\infty^3 A_s}, \quad \text{pitch efficiency:} \quad \eta_p = \frac{< \tau(t)\dot{\theta}(t) >}{0.5\rho U_\infty^3 A_s}, \tag{3}$$

where $\dot{h}(t)$ and $\dot{\theta}(t)$ are the heaving velocity and pitching velocity, respectively, and A_s is the swept area of the foil defined as the foil's maximum transverse excursion multiplied by the span [3,33].

B. Cyber-physical system

The elastically mounted hydrofoil can be treated as a spring-mass-damper system forced by a fluid force, F_{fluid}:

$$m\ddot{y} + b\dot{y} + ky = F_{\text{fluid}}, \tag{4}$$

where y is the displacement in the heave direction, m is the hydrofoil mass, and b and k are the damping and spring stiffness of the mounting system. At a Reynolds number of $\mathcal{O}(10^4)$, the inertial force from the fluid, $0.5\rho U_\infty^2 sc$, is assumed to be the dominant scaling force [30] and based on this assumption, we nondimensionalize the governing Eq. (4):

$$m^*\ddot{y}^* + b^*\dot{y}^* + k^* y^* = C_F, \tag{5}$$

where $y^* = y/c$ is the scaled heave amplitude, $C_F = F_{\text{fluid}}/(0.5\rho U_\infty^2 sc)$ is the coefficient of the fluid forcing, and the nondimensional parameters are given by

$$b^* = \frac{b}{0.5\rho U_\infty sc}, \tag{6}$$

$$k^* = \frac{k}{0.5\rho U_\infty^2 s}, \quad \text{and} \tag{7}$$

$$m^* = \frac{m}{0.5\rho c^2 s}. \tag{8}$$

Instead of using physical springs and dampers to achieve the elastic mounting in the heave direction, we employed a cyber-physical system that simulates the properties of the springs and dampers by implementing a force-feedback control system [25,26,28,30,34]. The cyber-physical system is schematically illustrated in Fig. 1(c). The fluid forces on the hydrofoil are measured and used as input to the feedback control system. The target heaving position output is determined by the integrated contribution of both the fluid forces and the structural forces (forces due to the springs, dampers and mass). Similar to the CPFD control system presented by Mackowski and Williamson [26], we start the force analysis with the Newton's law, $F = ma$, where F is the force that determines the motion of interest, and includes both the measured fluid force and the virtual elastic force computed in the control system:

$$F_{\text{fluid}} + F_{\text{virtual}} = ma, \tag{9}$$

where $F_{\text{virtual}} = -m\ddot{y} - b\dot{y} - ky$ is the structural forces, simulating a spring-mass-damper system. In contrast to Mackowski and Williamson's implementation, however, we integrate Eq. (9) twice to obtain the target discreet position output, Δy, for the flow-induced heave motion:

$$\iint_{t_0}^{t_0+\Delta t} F_{\text{fluid}} + F_{\text{virtual}}\, dt = m\Delta y. \tag{10}$$

One benefit of this approach is that noise in the measured force can be reduced significantly by the integration, thus avoiding the use of filters and the filter-related phase delay. Another benefit is that the system becomes more robust and less sensitive to disturbance after the use of twice integration.

Similar to the studies of elastically mounted cylinders [25,35], the fluid force in Eq. (4) can be decomposed into two components: one in phase with the foil velocity ($\dot{y}$) and the other in phase with the foil acceleration ($\ddot{y}$). For illustrative purposes, we can assume a sinusoidal flow-induced displacement and fluid force, $y(t) = H_0 \cos(\omega t)$ and $F_{\text{fluid}} = F_0 \cos(\omega t + \phi)$, where ϕ is the phase difference between the fluid force and the displacement. Then the fluid force can be rewritten as the following:

$$F_{\text{fluid}} = \frac{F_0 \sin\phi}{H_0\omega}\dot{y} - \frac{F_0 \cos\phi}{H_0\omega^2}\ddot{y}. \tag{11}$$

The first term is related to the fluid damping effect (in phase with the velocity) while the second term contributes to the added mass effect (in phase with the acceleration). Substituting this into the equations of motion [Eq. (4)], rearranging the terms and nondimensionalizing as described above, we obtain

$$\left(m^* + \frac{H_0^* C_{F_0} \cos\phi}{\pi^2 St^2}\right)\ddot{y}^* + \left(b^* - \frac{C_{F_0} \sin\phi}{\pi St}\right)\dot{y}^* + k^* y^* = 0, \tag{12}$$

where $St = 2fH_0/U_\infty$ is the Strouhal number, $C_{F_0} = F_0/0.5\rho U_\infty^2 sc$ and $H_0^* = H_0/c$. From this we can see that both the fluid damping and the added mass terms are related to the phase difference between the heaving motion and the fluid forcing, ϕ. It should be noted that when the system reaches a steady state motion, Eq. (12) inherently requires the damping term to vanish (the fluid damping cancels out the physical damping b). From the perspective of energy budget, it is clear to see that a steady state motion indicates that the energy extracted from the fluid (through negative fluid damping) is completely dissipated by the physical damping so that the total energy in the system remains unchanged. This will become important later in the discussion of the energy harvesting performance with respect to phase.

Equation (12) also highlights the role of added (fluid) mass to the dynamics of the system. At steady state, when the effective damping is zero, the natural frequency of oscillation is determined from the combination of stiffness and both the physical and added mass. The current experiments were conducted with a relatively large mass ratio, $m^* \sim 5$, and we therefore expect the physical mass to dominate over the added mass and the resonant frequency of the system to be close to the structural frequency, $2\pi f_n = \sqrt{k/m}$. However, it is also worth noting that even for low mass ratios, the role of added mass can change dramatically with the phase between the hydrofoil motion and the fluid forcing due to the $\cos\phi$ dependency in Eq. (12).

Validation

"Ring-down" experiments, using different elastic parameters (mass, stiffness, and damping), were performed to validate the system behavior. As an example, Fig. 1(d) shows the ring-down response with a fixed set of elastic parameters (stiffness $k = 200$ N/m, damping $b = 5$ kg/s and mass $m = 8.5$ kg), performed in the air. Due to the cyber-physical mass, stiffness and damping, the foil exhibits a damped oscillatory decay back to its neutral position. The measured heave position in the "ring-down" experiment is then compared with the theoretical position outputs using the same elastic parameters [Fig. 1(d)]. The results from the ring-down experiments show that the

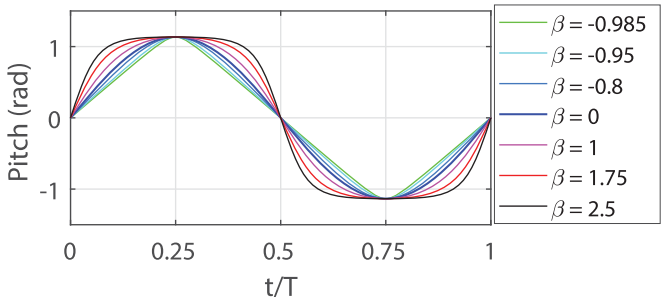

FIG. 2. Nonsinusoidal pitch profiles: $-1 < \beta < 0$ for triangular profiles; $\beta = 0$ for sinusoidal and $\beta > 0$ for trapezoidal profiles.

experimental measurement matches the theoretical position well (phase lag less than 5 degrees), even when the motion amplitude is small. As reported by Mackowski and Williamson [26], a phase lag of five degrees at the system's natural frequency generates no significant change in the experimental vibration response.

C. Nonsinusoidal pitch profiles

Several researchers [e.g., 3,11,12] have reported on the energy harvesting performance of a hydrofoil with a fully prescribed sinusoidal and nonsinusoidal motion. In these experiments we also explored both sinusoidal and nonsinusoidal pitch profile effects on the power extraction performance of an elastically mounted hydrofoil. Adopting the definition from Lu *et al.* [14], the nonsinusoidal pitch profiles are defined as

$$\theta(t) = \begin{cases} \frac{\theta_0 \sin^{-1}[-\beta \sin(2\pi f t)]}{\sin^{-1}(-\beta)}, & -1 \leqslant \beta < 0, \\ \theta_0 \sin(2\pi f t), & \beta = 0, \\ \frac{\theta_0 \tanh[\beta \sin(2\pi f t)]}{\tanh(\beta)}, & \beta > 0, \end{cases}$$

where β is a parameter characterizing the shape of the pitch profile: triangular ($-1 < \beta < 0$), sinusoidal ($\beta = 0$) and trapezoidal ($\beta > 0$) as shown in Fig. 2. As discussed by Lu *et al.* [36], β serves as a measure of the rate of change in pitch reversal; a larger β suggests a faster pitching rate and a larger pitching acceleration. This will be revisited later in the discussion of nonsinusoidal profile effects on energy harvesting performance.

D. Parametric variations

In the current manuscript, we first present results from a parametric sweep over a large range of stiffness (from 0 to 450 N/m) and damping (from 3.5 to 30 kg/s) for a fixed mass ratio and using a sinusoidal pitch profile ($\beta = 0$). By varying the actuated pitch frequency and damping, the effects of reduced frequency and damping coefficient are discussed in detail to understand the optimal parameters for energy harvesting performance. In the last part of the paper, the effects of different prescribed pitch profiles on energy harvesting are discussed on the energy harvesting performance.

III. RESULTS AND DISCUSSION

A. Parametric sweep of frequency ratio and damping coefficient

With a fixed sinusoidal pitch motion profile and a constant mass ratio of 4.9, a parametric sweep with respect to the stiffness, k, and the damping, b, were carried out to investigate the response of the flow-induced heaving motion and the resulting power extraction performance of the elastically

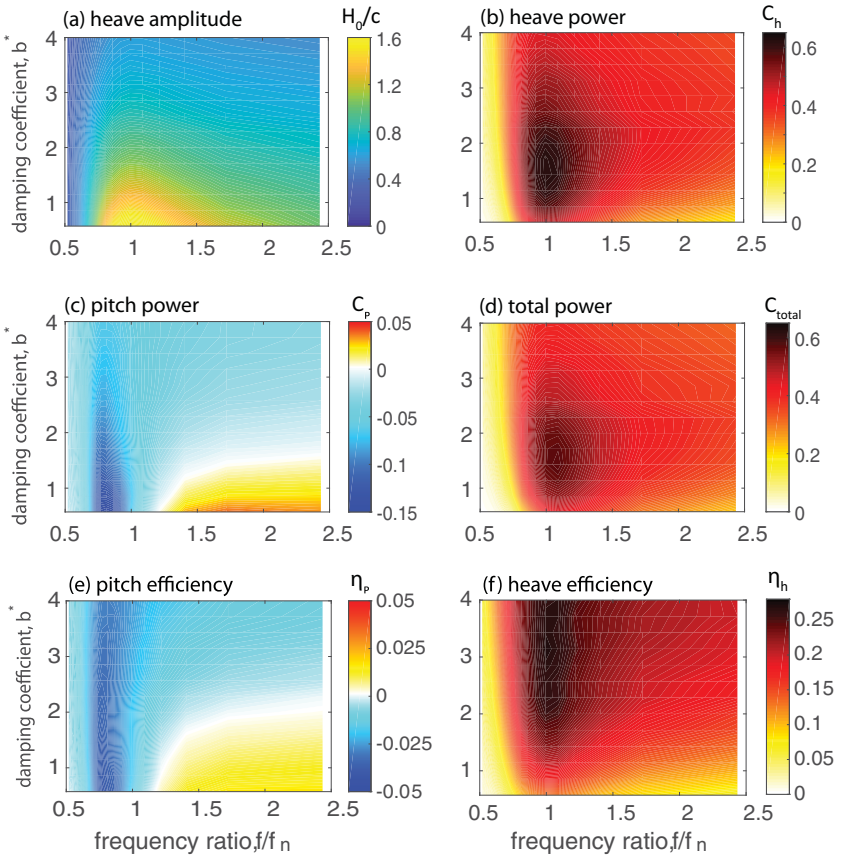

FIG. 3. Contour plots of (a) induced heave amplitude, H_0, (b) heave power coefficient, C_h, (c) pitch power coefficient, C_p, and (d) total power coefficient, C_{total}, (e) pitch efficiency, η_p, (f) heave efficiency, η_h, with respect to frequency ratio, f/f_n, and damping coefficient, b^*; parameters: prescribed sinusoidal pitch profile with pitch amplitude, $\theta_0 = 65^\circ$.

mounted hydrofoil. Results of the parametric sweep (Fig. 3) illustrate (a) the flow-induced heave amplitude, H_0, (b) the heave power coefficient, C_h, (c) the pitch power coefficient, C_p, (d) the total power coefficient, C_{total} (sum of the heave and pitch components), (e) the pitch efficiency, η_p, and (f) the heave efficiency, η_h.

First, for a fixed value of the frequency ratio, the induced heave amplitude is shown to decrease with damping coefficient. When varying the frequency ratio at a fixed damping coefficient, the maximum induced heave amplitude was observed around frequency ratio $f/f_n = 1$, which is usually referred as the resonant phenomenon [35]. This resonance suggests that, at this frequency, the preferred vortex shedding frequency is identical to the natural frequency of the energy harvester. A precipitous drop in the heave amplitude and the heave power is observed at $f/f_n < 1$, while the decrease is more smooth for $f/f_n > 1$ [Figs. 3(a) and 3(b)].

Second, when comparing the heave and pitch power coefficients [Figs. 3(b) and 3(c)], one can see that the heave power component is generally much larger than the pitch power component, particularly when the frequency ratio is close to 1. Therefore, the power extracted from the heave motion dominates the energy harvesting process, a result consistent with the results in literature using a prescribed oscillating hydrofoil [2,3,33]. For the most part, the pitch power is slightly negative except for a small region with small damping coefficient and high frequency ratio.

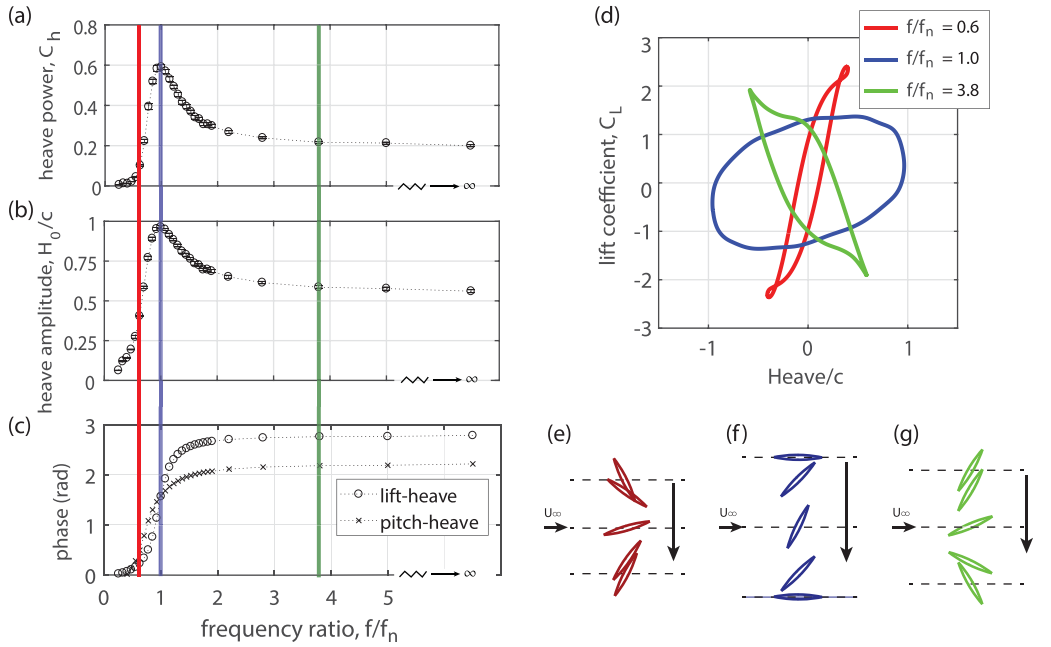

FIG. 4. Response of (a) heave power coefficient, (b) flow-induced heave amplitude, and (c) phase difference between the lift force and the flow-induced heave motion (circles ○) and phase difference between the prescribed pitch motion and the flow-induced heave motion (cross ×) at a fixed damping coefficient of 1.5; (d) lift-heave portraits for three different frequency ratios: $f/f_n = 0.6$ (red), $f/f_n = 1.0$ (blue), $f/f_n = 3.8$ (green). Foil kinematics in half a cycle: (e) $f/f_n = 0.6$ (red), (f) $f/f_n = 1.0$ (blue), (g) $f/f_n = 3.8$ (green).

Thirdly, a clearly defined peak in the heave power coefficient is observed at the frequency ratio around 1, and the damping coefficient around 1.5 [Fig. 3(b)]. However, the maximum power loss due to pitch appears around frequency ratio of 0.8 [Fig. 3(c)], which is likely due to the high torque required to rotate the hydrofoil in the presence of a strong leading edge vortex (LEV) that forms as the blade reaches its peak heave amplitude. This conjecture is supported by the PIV measurements from Kim *et al.* [3], which showed that a poorly positioned LEV on the hydrofoil resulted in energy loss in the pitch performance. Thus, in general a high net power extraction output is achieved, as shown in Fig. 3(d), with the frequency ratio for peak performance slightly larger than 1. Since the heave power component contributes most of the power extracted from the flow, in the rest of the paper, we will focus on the energy harvesting performance of the flow-induced heaving motion.

Last, the pitch efficiency [Fig. 3(e)] is small and slightly negative for most part, while the heave efficiency [Fig. 3(f)] is positive, reaching a maximum at the frequency ratio around 1 and, in general, much larger than the pitch component. However, instead of a clearly defined peak in the heave power coefficient [Fig. 3(b)], the heave efficiency [Fig. 3(f)] shows a flat peak at damping coefficient $b^* > 2$. This is not surprising considering that the flow-induced heave amplitude (which appears in the denominator of the efficiency definition) decreases with increasing damping coefficient, thus compensating the drop in the power extraction and resulting in a high efficiency performance [Eq. (3)].

B. Frequency ratio effects

In this section, a specific case with a fixed damping coefficient of $b^* = 1.5$ is examined in more detail to better understand the effect of the frequency ratio on the flow-induced heaving motion and the power extraction performance. Figure 4 shows the response of (a) the heave power coefficient,

C_h, (b) the heave amplitude, H_0, and (c) the phase difference between the lift force and the flow-induced heave and the phase difference between the prescribed pitch motion and the flow-induced heave motion. The force portrait in Fig. 4(d) shows the lift-heave relation, in which the area enclosed by the curve denotes the work done by the lift force during a cycle.

Echoing the results from the full parameter sweep (Fig. 3) we see a sharp rise in both heave amplitude and heave power as the frequency ratio approaches one, while a more gentle decay is observed for frequencies above the resonance [Figs. 4(a) and 4(b)]. The broad resonant peaks in Figs. 4(a) and 4(b) signify strong damping in the system which is, of course, advantageous for energy harvesting since "damping" represents energy extracted from the flow. Consistent with classical second-order linear system theories, a phase jump around π is observed as the system passes through resonance [Fig. 4(c)].

Figure 4(d) shows the lift force portrait for three different frequency ratios, with the curve-enclosed area representing the energy extracted by the foil in a cycle. When the frequency ratio is smaller than one (the red color scheme in Fig. 4), the phase difference between pitch and heave is close to 0, away from the optimal phase of $\pi/2$ [Fig. 4(c)]. In this case, the lift force reaches its maximum value at the end of the heave stroke, where the angle of attack (AOA) is large but the heave velocity is at its minimum [Fig. 4(e)], resulting in low energy extraction performance [Fig. 4(d)]. Similar results are observed when the frequency ratio is much larger than 1 (the green color scheme) when the lift force leads the heave motion. In both cases the peak hydrodynamic lift force is produced at the pitch reversal points where the heave velocity is low due to the poor phase synchronization. In these suboptimal cases, the phase portraits of power extraction are compressed [the red and green curves in Fig. 4(d)] and the amplitude of the flow-induced heave motion is small since not enough power is extracted from the fluid to sustain the passive heave motion.

In contrast to these cases, when the frequency ratio is close to one (the blue color scheme), a phase difference of $\pi/2$ is produced between the lift and the flow-induced heave motion and also between the prescribed pitch motion and the flow-induced heave motion [Fig. 4(c)], and with this phase synchronization, a peak power coefficient is achieved together with the maximum flow-induced heave amplitude [Figs. 4(a) and 4(b)]. This is also reflected in the phase portrait which exhibits a maximum enclosed area [blue, Fig. 4(d)], indicating maximum energy harvesting per cycle. This optimal phase synchronization is in agreement with other published results [1,4,37]. Using a hydrofoil with both prescribed heaving and pitching motions, those researchers report that a phase difference of $\pi/2$ ensures a good force-velocity synchronization for energy extraction. Here we achieve peak performance with only prescribed pitching motion.

As discussed by Hover *et al.* [25,38] and also shown in Eqs. (11) and (12), the lift force can be divided into two components: $C_{Lv} = C_L \sin\phi$, in phase with the heave velocity and serving as a damping factor, and $C_{La} = -C_L \cos\phi$, which is in phase with the acceleration and serves as an added mass factor. As before, ϕ is the phase difference between the lift force and the heave motion. Since the power is calculated from the product of the lift force and the heave velocity [Eq. (2)], positive values of C_{Lv} are associated with energy extraction from the flow. One can see from the above two components that C_{Lv} reaches its maximum value at $\phi = \pi/2$, producing the largest excitation (heave amplitude) and highest performance of energy extraction, in agreement with the current observations [Fig. 4(a) and 4(b)]. At the same time, and as previously highlighted in Eq. (12), when $\phi = \pi/2$, we see that the added-mass factor (C_{La}) vanishes, confirming that the added mass effect is small at this resonant condition. This is further validated in our experimental observation that the maximum flow-induced heave amplitude and heave power are achieved at frequency ratio $f/f_n \sim 1$ (Fig. 4), where the natural frequency, f_n is based solely on the structural support of the hydrofoil.

In particular, as the frequency ratio becomes very large (stiffness $k \sim 0$), the energy harvesting performance is far from the optimum [Fig. 4(a)], which contradicts the numerical results that zero stiffness produces the optimal performance of energy extraction [21]. This discrepancy may be due to the fact that the linear model in Zhu's simulation [21] does not include the mass and inertial of the foil, and hence does not exhibit a natural frequency. The above analysis of the frequency

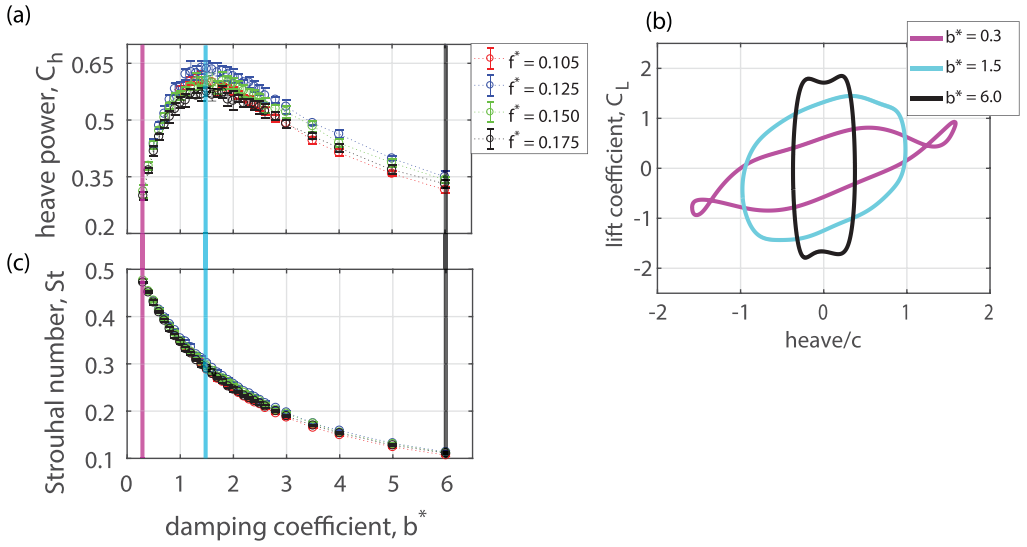

FIG. 5. At a fixed frequency ratio ($f/f_n = 1$), (a) the heave power coefficient, C_h, is plotted with respect to damping coefficient; (b) the lift-heave portrait demonstrates the work done by the lift force for different damping coefficient, $b^* = 0.3$, 1.5, and 6.0, at a reduced frequency $f^* = 0.150$; (c) the Strouhal number, $\mathrm{St} = 2fH_0/U_\infty$, is plotted with respect to damping coefficient, b^*, for different reduced frequency, $f^* = fc/U_\infty$.

ratio effects on the energy harvesting performance is based on a mass ratio around 5 ($m^* = \frac{m}{0.5\rho c^2 s}$). Further experiments with different mass ratio (m^* varying from 3 to 15) confirm that the optimal frequency ratio for energy harvesting is $f/f_n = 1$ (results not shown here).

C. Damping coefficient effects

As discussed earlier, in Sec. III A, the damping coefficient plays an important role in determining the amplitude of the flow-induced heave motion and the related energy harvesting performance. To further understand the damping effects, in this section, we discuss experiments conducted at different reduced frequencies but varying the stiffness of the heave mounting so that the frequency ratio was held constant at a value of 1. Figure 5(a) shows the heave power coefficient, C_h, as a function of damping coefficient, b^*, at four different reduced frequencies. For each reduced frequency tested, the peak performance of energy harvesting is achieved at the damping coefficient of 1.5, confirming the observation of the optimal damping coefficient in Sec. III A. The results also indicate that the peak in the heave power coefficient has a weak, nonmonotonic dependence on the reduced frequency, f^*, rising to a maximum near $f^* = 0.125$ and then decreasing at large reduced frequencies. This agrees well with the experimental results from Kim *et al.* [3]. This f^*-dependence will become important in Sec. III C 1, where we present a model for the power coefficient.

Lift-heave phase portraits for three representative damping coefficients are presented in Fig. 5(b), with the extracted energy per cycle represented by the area enclosed by the curves. For small damping (the pink color scheme), the induced heave amplitude is large (more than 1.5 chord lengths), but the lift force throughout the energy harvesting cycle is small, resulting in a low power extraction coefficient [Fig. 5(a)]. In addition, a negative hysteresis is observed near the maximum heave positions, which puts energy back into the flow, similar to the negative hysteresis observed by Onoue *et al.* [30] for a pitching flat plate. As indicated by Onoue and Breuer's PIV results [31], the negative hysteresis in the current study suggests that the LEV detaches from the foil, causing the lift force to drop. However, a second LEV starts to form before the heave cycle is complete, causing

the lift force to rise again near the top of the stroke. That second LEV impedes the return motion of the foil, transferring energy back into the flow.

By contrast, for a large damping coefficient (the black color scheme), the induced heave amplitude is small (less than 0.5 chord lengths), and although a high lift force is generated, the overall power coefficient is again small, this time due to the low heave velocity. At the optimal damping coefficient of 1.5 (the cyan color scheme), the largest enclosed area is produced by a modest lift force and a heave amplitude about one chord length [Fig. 5(b)]. This optimal heave amplitude (about one chord length) is in agreement with the results found using a prescribed pitching and heaving hydrofoil [2–4].

Scaling of the Strouhal number

In addition to the power extraction performance, another output from the semipassive energy harvester is the Strouhal number, $\mathrm{St} = 2fH_0/U_\infty$, where H_0 is the flow-induced heave amplitude. As shown in Fig. 5(c), the Strouhal number exhibits a monotonic dependence on damping but collapses extremely well over a range of reduced frequencies between 0.105 and 0.175. Not only does the response of the power and Strouhal number scale with damping, but at the optimal damping coefficient ($b^* = 1.5$), the elastically mounted system produces and maintains a Strouhal number of 0.3, which is also observed as the optimal value in literature [2,4]. We can fit this Strouhal number data with an empirical equation:

$$\mathrm{St} = 0.27e^{-0.94b^*} + 0.28e^{-0.16b^*}, \tag{13}$$

which will be used in the development of a theoretical model later in this section. To understand the collapse of the Strouhal number, we define the nominal effective angle of attack (AOA) of the foil to the flow,

$$\theta_{e0} = \theta_0 - \arctan(V_{h0}/U_\infty), \tag{14}$$

which accounts for the contributions from the pitch amplitude, θ_0, and the maximum heave velocity, V_{h0}. As the flow-induced heave motion is quasiharmonic (the first Fourier mode accounts for 95% of the observed heave kinematics), we can approximate the heave motion as sinusoidal, thus the maximum heave velocity can be estimated as $V_{h0} = 2\pi fH_0$. Considering the definition of the Strouhal number, the nominal effective AOA can be rewritten as $\theta_{e0} = \theta_0 - \arctan(\pi\,\mathrm{St})$, which indicates that, at a fixed frequency ratio of 1 and for a fixed damping coefficient, the time history of the effective angle of attack is also fixed over a wide range of physical parameters. This result finds its counterpart in the experimental results of Baik *et al.* [10]. By varying the reduced frequency and heave amplitude while keeping the same effective AOA of the foil to the flow, Baik *et al.* [10], using PIV measurements, found that the trajectories of the LEV were identical for the range of parameters explored, suggesting that, in the current study, the LEV trajectories should also be identical for different reduced frequencies (but the same Strouhal number). This conjecture will be tested in future experiments that measure the flow fields.

The same dynamic similarity should also be observed in the hydrodynamic forces acting on the foil, and this assertion is confirmed in Fig. 6, which shows an excellent collapse in both the lift coefficient [Fig. 6(a)] and the torque coefficient [Fig. 6(b)], especially during the first part of the cycle, $t/T = 0 - 0.25$. We do see minor differences in the hydrodynamic forces at different frequencies during the latter part of the cycle, $t/T = 0.25$–0.5, but they are small and do not appear to follow any consistent trend. However, during $t/T = 0.25$–0.5, one can see [Fig. 6(b)] that the peaks in the torque coefficient are higher and appear later in the cycle for larger reduced frequencies. This higher peak in torque can be attributed to the increased added-mass effect at larger pitching reduced frequencies, which is supported by Rival *et al.* [17] and Eldredge and Jones [8], who reported that the noncirculatory (added-mass) contribution to the hydrodynamic forces was related to the inertial reaction of the fluid and thus increased with the reduced frequency. This reduced frequency dependency is also observed by Baik *et al.* [10], who demonstrated that, with

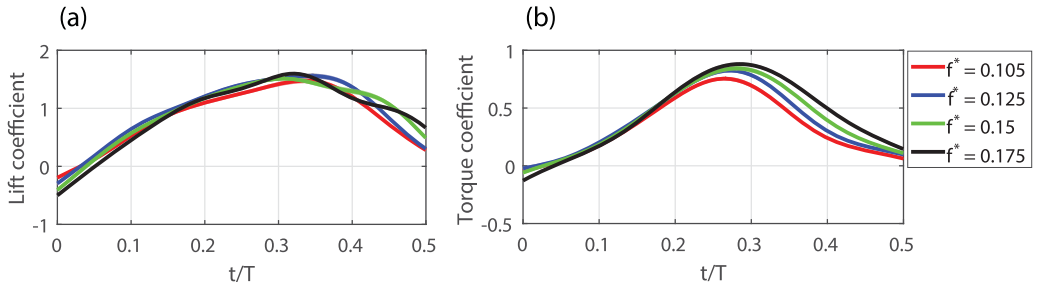

FIG. 6. Temporal evolution of (a) lift coefficient and (b) torque coefficient for different reduced frequencies, at a fixed frequency ratio of 1 and a fixed damping coefficient of 1.5. Data of half a cycle are shown for simplicity due to the dynamic symmetry.

the same effective AOA history, the observable trend of the force histories was strongly associated to the Strouhal number, with small modifications due to reduced frequency—similar to the present observations of forces in Fig. 6. In addition, Onoue *et al.* [32] reported that an increase in reduced frequency helped to mitigate the drift of the LEV core toward the trailing edge, thus delaying the vortex separation from the hydrofoil. This delayed movement of the LEV core due to the reduced frequency explains the late peaks in the torque coefficient for high reduced frequencies [Fig. 6(b)] in the current study.

D. Comparisons with a reduced-order model

The insights discussed in the previous sections can be incorporated into a simple model that helps to understand the behavior of this energy-harvesting system. From classical vibration theory, power dissipated by the damper in a forced oscillator is given by $b\dot{h}^2(t)$ [39]. Normalizing the damper dissipation by the kinetic energy flux in the oncoming flow, $0.5\rho U_\infty^3 sc$, we can write the power extraction coefficient for the heave motion as

$$C_h = \frac{< b\dot{h}^2(t) >}{0.5\rho U_\infty^3 sc}. \tag{15}$$

Considering the definition of damping coefficient [Eq. (6)] and assuming a sinusoidal flow-induced heave motion, $h(t) = H_0 \sin(2\pi ft)$, where f and H_0 are the heave motion frequency and amplitude, respectively, the power coefficient [Eq. (15)] can be rewritten as

$$\begin{aligned} C_h &= \frac{b}{0.5\rho U_\infty sc}\left(\frac{2\pi fH_0}{U_\infty}\right)^2 < \cos^2(2\pi ft) > \\ &= 0.5b^*(\pi \mathrm{St})^2, \end{aligned} \tag{16}$$

where $\mathrm{St} = 2fH_0/U_\infty$ is the Strouhal number.

Since the Strouhal number is a universal function of the damping coefficient (Fig. 5), we can substitute the empirically determined equation for the Strouhal number [Eq. (13)] into the equation for the power coefficient and express the heave power coefficient C_h solely as a function of the damping coefficient, b^*. Doing so, and taking the derivative of that function with respect to b^*, we find that the maximum heave power coefficient is achieved at $b^* = 1.46$, which agrees very well with the observation ($b^* \sim 1.5$) in the experiments (Fig. 3, Sec. III A.)

The equation for the power coefficient [Eq. (16)] also suggests a linear scaling with damping coefficient, a prediction confirmed by the experimental data over all frequencies tested (Fig. 7). The slope of the experimental data, though linear, is slightly smaller than that predicted by the theoretical model, a discrepancy probably due to the breakdown of the assumption of a sinusoidal heave motion, which is observed to be less accurate as the damping coefficient becomes large.

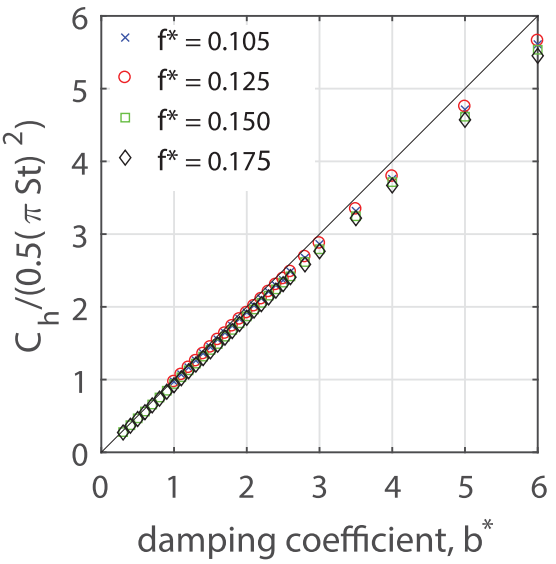

FIG. 7. Relationship between heave power coefficient, scaled by the Strouhal number squared, and the damping coefficient. Solid line: theoretical prediction [Eq. (16)]; symbols: experimental results at several frequencies, all at a fixed frequency ratio of 1.

E. Nonsinusoidal pitching profiles effects on energy harvesting

It has been reported that nonsinusoidal motion profiles can potentially increase the energy harvesting performance of a flapping hydrofoil by changing the effective angle of attack of the foil and the resulting vortex dynamics and hydrodynamic forces [11–15]. In the current study, we will focus on the nonsinusoidal pitch kinematics since the pitch motion is prescribed while the the heave motion is flow-induced (elastically mounted). In addressing the effects of the pitching kinematics, we first revisit the effect of frequency ratio, f/f_n, and damping coefficient, b^*, and expand on our earlier observation (Fig. 3) that the optimal performance of energy extraction is achieved at the frequency ratio of 1 and damping coefficient of 1.5. We now see that this result is maintained for different pitching profiles (Fig. 8). However, the pitch profile has a significant effect, particularly near the optimal performance region ($f/f_n = 1$ and $b^* = 1.5$). Comparing the energy harvesting performance between different pitching profiles, we see from Fig. 8 that the triangular pitch profiles ($-1 < \beta < 0$) reduce the power extraction performance, compared to the sinusoidal pitch profile, while the trapezoidal profiles ($\beta > 0$) increase the power coefficient.

If we look into this with finer resolution, then we can vary the profile parameter β at a fixed frequency and damping ($f/f_n = 1$ and $b^* = 1.5$), and we see (Fig. 9) that the heave power performance is improved by the trapezoidal pitch profiles ($\beta > 0$) compared with the sinusoidal profile ($\beta = 0$), which is in agreement with the numerical results of Xiao *et al.* [16]. The power coefficient reaches 0.9 at $\beta \sim 2$—a 50% improvement over the sinusoidal performance—before levelling off. In contrast, the triangular pitch profiles ($-1 < \beta < 0$) reduce the heave power output especially with a precipitous drop observed at $-1 < \beta < -0.75$. The heave power coefficient predicted using our simple theoretical model [Eq. (16)] is also presented and compared with the measured heave power coefficient [Fig. 9(a)]. The good agreement between the two curves validates the utility of the model, even for different pitch profiles, ranging from triangular to trapezoidal profiles. It is not surprising that the prediction lies slightly above the experimental values, considering that the measured flow-induced heave profile is not purely sinusoidal, which is assumed by the model.

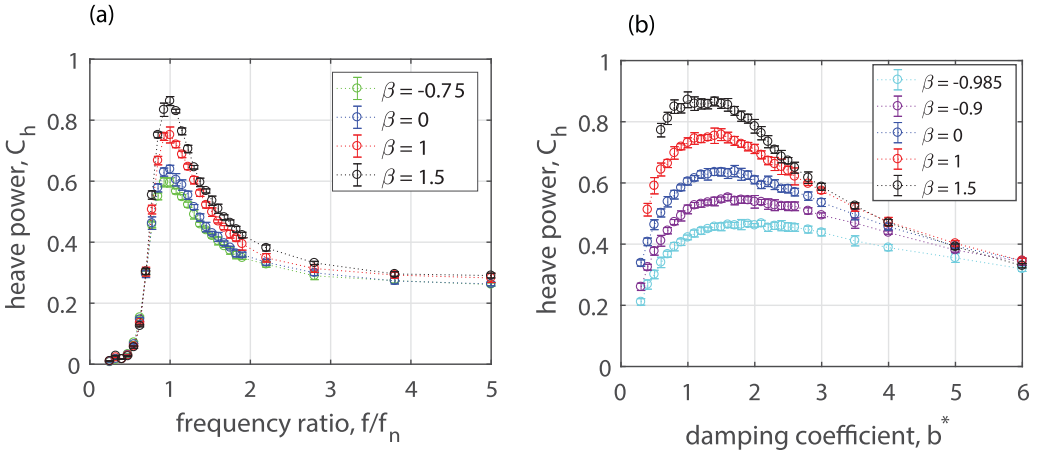

FIG. 8. (a) Heave power coefficient as a function of frequency ratio, f/f_n, at different pitch profiles (β); (b) heave power coefficient as a function of damping coefficient, b^*, at different pitch profiles (β).

It is perhaps unsurprising that the pitch power loss increases with β [Fig. 9(b)] since more power is required to initiate the faster pitch reversal in the trapezoidal pitch profiles [11]. However, such power loss (for example, -0.08 at $\beta = 2.5$) is much smaller than the improvement in the heave power (0.30 at $\beta = 2.5$), resulting in a net improvement in the total power output in trapezoidal pitch profiles [the cyan line in Fig. 9(a)]. This loss-gain tradeoff is eventually lost at large values of β, and by $\beta = 2.25$, the cost associated with the increased negative pitching power is greater than the benefit associated with the improved positive heave power, resulting in a levelling off and eventual decline in the total power coefficient [the cyan line in Fig. 9(a)].

Figure 9(c) shows the lift-heave phase portrait for three different pitching profiles as identified in Fig. 9(a). With the extracted energy per cycle represented by the enclosed area, Fig. 9(c) confirms the previous result that the trapezoidal pitch profile (the green curve) extracts much more energy in a cycle than the sinusoidal (the blue curve) and triangular (the red curve) profiles, consistent with the power coefficient [Fig. 9(a)]. In addition, we can see from Fig. 9(c) that the increment of power

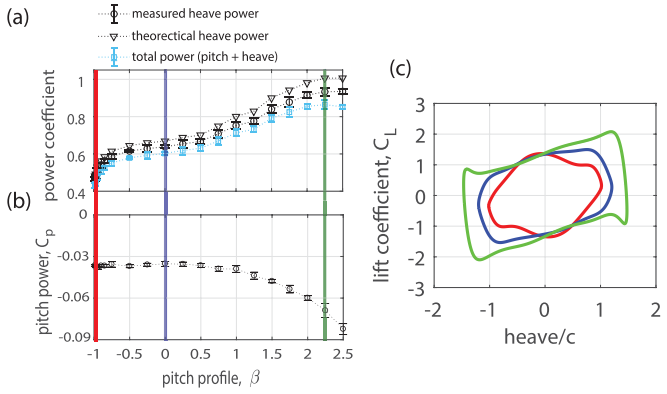

FIG. 9. (a) Heave power coefficient measured in the experiment and predicted by the theoretical model [Eq. (16)] and total power coefficient measured in the experiment, (b) pitch power coefficient, and (c) lift-heave phase portrait. Parameters: reduced frequency $f^* = 0.125$, frequency ratio, $f/f_n = 1$, damping coefficient, $b^* = 1.5$.

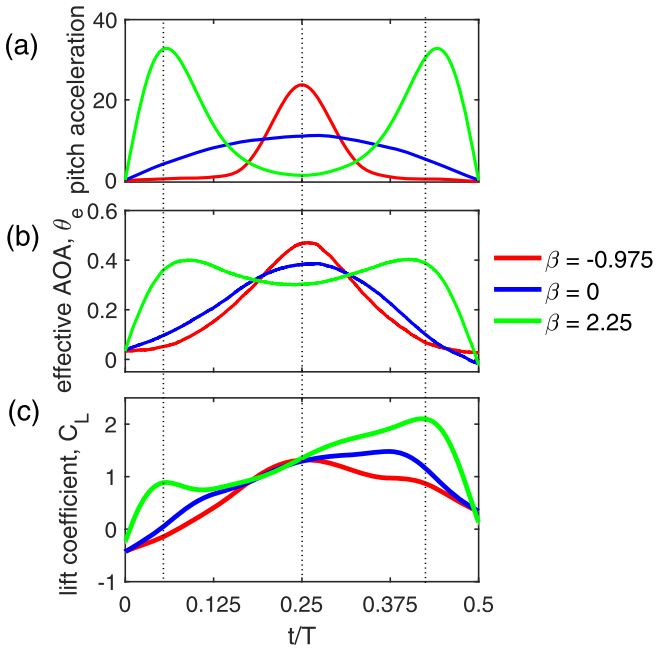

FIG. 10. Instantaneous (a) pitch acceleration (rad/s^2), (b) effective AOA, and (c) lift coefficient are shown for three pitch profiles ($\beta = -0.975$ (triangular), 0 (sinusoidal), and 2.25 (trapezoidal), for half cycle). The instantaneous effective AOA is given by $\theta_e(t) = \theta(t) - \arctan(V_h(t)/U_\infty)$, where $V_h(t)$ is the instantaneous heave velocity. Parameters: reduced frequency, $f^* = 0.125$, frequency ratio, $f/f_n = 1$, damping coefficient, $b^* = 1.5$.

output comes from two parts: the increase in the flow-induced heave amplitude and the enhancement of lift force, which will be discussed in detail later in this section.

As seen in Sec. III C 1, the effective angle of attack (AOA) plays an important role in the hydrodynamic force production and similar effective AOA histories are accompanied by similar hydrodynamic forces on an oscillating hydrofoil. To understand the hydrodynamic origins of the lift force enhancement associated with the different pitch profiles, time histories of the pitch acceleration, lift coefficient, and the associated instantaneous effective AOA are shown in Fig. 10. For all three pitch profiles, we see two peaks in the lift coefficient, one early in the half-cycle, the second towards the end of the half-cycle. This is similar to the trends observed by Deng *et al.* [19] and Teng *et al.* [15].

Early in the cycle, $t/T < 0.18$, the LEV is weak, and we expect that it does not contribute very much to the lift force. Here, we see that the the triangular profile ($\beta = -0.975$, red line) is almost completely in phase with the effective AOA, θ_e, and the pitch acceleration is negligible, suggesting that the dominant mechanism for lift generation is quasisteady. As β increases (corresponding to a larger pitch acceleration), the force due to the added mass ("noncirculatory lift" [6,40–42]) becomes important and the lift coefficient rises more quickly. This explanation is supported by the observation that, for the trapezoidal pitch profile (green curves), the maximum in lift occurs at the same time as the maximum in pitch acceleration ($t/T = 0.06$) and before the maximum in the effective angle of attack, θ_e ($t/T \sim 0.09$).

As time increases, the lift force continues to rise, reflecting the importance of the LEV which is growing on the upper surface of the foil and generates an unsteady circulatory lift force. The LEV strength is greatest in the case of the trapezoidal pitch profile [18,19] and this is reflected in the high C_L during this part of the cycle ($t/T > 0.25$). In the case of the triangular pitch profile, the LEV

grows more slowly, but the mid-cycle peak in the pitch acceleration contributes to an additional noncirculatory "bump" in the lift force at $t/T \sim 0.25$ which compensates for the weak circulatory lift generated by the LEV.

Finally, the lift force drops precipitously at the end of the half-cycle. Here the decrease in C_L is not consistently associated with any feature in the pitch acceleration or the effective angle of attack, confirming previous results that show that the drop in force is related to the shedding of the LEV from the foil [3,6,10], which is not easily associated with the pitch profile.

IV. CONCLUSIONS

In this paper, the power extraction performance of a semipassive energy harvester was studied using a hydrofoil with a prescribed pitch motion and an elastically mounted heave motion achieved using a cyber-physical support. The power of the cyber-physical system allowed for a broad parametric sweep over the stiffness and damping to explore the performance of the semipassive energy harvester. We found that the optimal energy harvesting performance was achieved at damping coefficient of 1.5 and at frequency ratio $f/f_n = 1$, the resonance condition, where the phase difference between the prescribed pitch and the elastically mounted heave is 90°, which agrees well with the results obtained using a fully prescribed foil [2–4,43]. In addition, at this resonance condition the Strouhal number (heaving amplitude) and the hydrodynamic forces were found to collapse remarkably well for different reduced frequency tested ($f^* = 0.105 \sim 0.175$), suggesting a similarity in the vortex dynamics maintained in the elastically mounted system.

Effects of nonsinusoidal pitch profiles on energy harvesting performance were also reported, and it is found that the triangular pitch profiles ($-1 < \beta < 0$) were not as effective as the the sinusoidal pitch profiles ($\beta = 0$), while using the trapezoidal pitch profiles extracted more energy per cycle than the with the sinusoidal pitch profile, in line with the previous results [11,14]. In addition, the optimal trapezoidal pitch profile was found at $\beta = 2.25$, with over 50% improvement in the power coefficient compared with the sinusoidal pitch profile. This improvement was attributed to the lift force enhancement from both the noncirculatory force contribution related to the large pitch acceleration at the beginning of the stroke and the circulatory force contribution associated with a stronger LEV formation due to the large effective AOA maintained through most portion of the cycle.

To establish the connection between the hydrodynamic response in the elastically mounted system and the associated power extraction performance, we found that a simple model based on classical vibration theory was able to reproduce the observed maximum in the power coefficient, relying only on the observed scaling between the Strouhal number (i.e., the heave amplitude) and the system damping (i.e., energy harvested). The model agrees well with the measured results over a range of reduced frequency ($f^* = 0.105 \sim 0.175$) for both sinusoidal and nonsinusoidal pitch profiles. Nevertheless, to gain a deeper understanding of the observed scaling of the Strouhal number, measurements of the LEV dynamics (using, for example, PIV) will be performed in the future. Effects of nonlinear structural mounting (stiffness and damping) can also be explored to further improve the hydrodynamic response and the associated power extraction performance.

ACKNOWLEDGMENTS

The authors gratefully acknowledge the financial support from Advanced Research Projects Agency-Energy (ARPA-E), Grant No. DE-AR0000318, and the Air Force Office of Scientific Research (AFOSR), Grant No. FA9550-18-1-0322. We thank our colleagues in the Leading Edge team, particularly Jen Franck, Michael Miller, and Shreyas Mandre, for their insights and assistance.

[1] W. McKinney and J. DeLaurier, The Wingmill: An oscillating-wing windmill, J. Energy **5**, 109 (1981).

[2] T. Kinsey and G. Dumas, Parametric study of an oscillating airfoil in a power-extraction regime, AIAA J. **46**, 1318 (2008).

[3] D. Kim, B. Strom, S. Mandre, and K. Breuer, Energy harvesting performance and flow structure of an oscillating hydrofoil with finite span, J. Fluids Struct. **70**, 314 (2017).
[4] Q. Zhu, Optimal frequency for flow energy harvesting of a flapping foil, J. Fluid Mech. **675**, 495 (2011).
[5] T. Theodorsen, General theory of aerodynamic instability and the mechanisms of flutter, National Advisory Committee for Aeronautics, Report No. 496, 1935.
[6] C. W. Pitt Ford and H. Babinsky, Lift and the leading-edge vortex, J. Fluid Mech. **720**, 280 (2013).
[7] E. Limacher, C. Morton, and D. Wood, Generalized derivation of the added-mass and circulatory forces for viscous flows, Phys. Rev. Fluids **3**, 014701 (2018).
[8] J. D. Eldredge and A. R. Jones, Leading-edge vortices: Mechanics and modeling, Annu. Rev. Fluid Mech., **51**, 75 (2019).
[9] W. J. McCroskey, Unsteady airfoils, Annu. Rev. Fluid Mech. **14**, 285 (1982).
[10] Y. S. Baik, L. P. Bernal, K. Granlund, and M. V. Ol, Unsteady force generation and vortex dynamics of pitching and plunging aerofoils, J. Fluid Mech. **709**, 37 (2012).
[11] M. F. Platzer, M. A. Ashraf, J. Young, and J. C. S. Lai, Development of a new oscillating-wing wind and hydropower generator, in *Proceedings of the 47th AIAA Aerospace Sciences Meeting including the New Horizons Forum and Aerospace Exposition, Aerospace Sciences Meetings* (AIAA, Orlando, FL, 2009).
[12] M. A. Ashraf, J. Young, J. C. S. Lai, and M. F. Platzer, Numerical analysis of an oscillating-wing wing and Hydropower generator, AIAA J. **49**, 1374 (2011).
[13] J. Young, M. A. Ashraf, J. C. S. Lai, and M. F. Platzer, Numerical simulation of fully passive flapping foil power generation, AIAA J. **51**, 2727 (2013).
[14] K. Lu, Y. H. Xie, and D. Zhang, Nonsinusoidal motion effects on energy extraction performance of a flapping foil, Renew. Energy **64**, 283 (2014).
[15] L. Teng, J. Deng, D. Pan, and X. Shao, Effects of nonsinusoidal pitching motion on energy extraction performance of a semiactive flapping foil, Renew. Energy **85**, 810 (2016).
[16] Q. Xiao, W. Liao, S. Yang, and Y. Peng, How motion trajectory affects energy extraction performance of a biomimic energy generator with an oscillating foil? Renew. Energy **37**, 61 (2012).
[17] D. Rival, T. Prangemeier, and C. Tropea, The influence of airfoil kinematics on the formation of leading-edge vortices in bio-inspired flight, Exp. Fluids **46**, 823 (2009).
[18] I. Fenercioglu, B. Zaloglu, J. Young, M. A. Ashraf, J. C. S. Lai, and M. F. Platzer, Flow structures around an oscillating-wing power generator, AIAA J. **53**, 3316 (2015).
[19] J. Deng, C. P. Caulfield, and X. Shao, Effect of aspect ratio on the energy extraction efficiency of three-dimensional flapping foils, Phys. Fluids **26**, 043102 (2014).
[20] E. Shimizu, K. Isogai, and S. Obayashi, Multiobjective design study of a flapping wing power generator, J. Fluids Eng. **130**, 021104 (2008).
[21] Q. Zhu, M. Haase, and C. H. Wu, Modeling the capacity of a novel flow-energy harvester, Appl. Math. Model. **33**, 2207 (2008).
[22] Q. Zhu and Z. Peng, Mode coupling and flow energy harvesting by a flapping foil, Phys. Fluids **21**, 033601 (2009).
[23] H. Abiru and A. Yoshitake, Study on a flapping wing hydroelectric power generation system, J. Environ. Eng. **6**, 178 (2011).
[24] G. H. Huxham, S. Cochard, and J. Patterson, Experimental parametric investigation of an oscillating hydrofoil tidal stream energy converter, in *Proceedings of the 18th Australasian Fluid Mechanics Conference*, AFMC, Launceston, Australia, 2012.
[25] F. S. Hover, S. N. Miller, and M. S. Triantafyllou, Vortex-induced vibration of marine cables: Experiments using force feedback, J. Fluids Struct. **11**, 307 (1997).
[26] A. W. Mackowski and C. H. K. Williamson, Developing a cyber-physical fluid dynamics facility for fluid-structure interaction studies, J. Fluids Struct. **27**, 748 (2011).
[27] A. W. Mackowski and C. H. K. Williamson, An experimental investigation of vortex-induced vibration with nonlinear restoring forces, Phys. Fluids **25**, 087101 (2013).
[28] J. H. Lee, N. Xiros, and M. M. Bernitsas, Virtual damper-spring system for VIV experiments and hydrokinetic energy conversion, Ocean Eng. **38**, 732 (2011).

[29] J. H. Lee and M. M. Bernitsas, High-damping, high-Reynolds VIV tests for energy harnessing using the VIVACE converter, Ocean Eng. **38**, 1697 (2011).
[30] K. Onoue, A. Song, B. Strom, and K. S. Breuer, Large amplitude flow-induced oscillations and energy harvesting using a cyber-physical pitching plate, J. Fluids Struct. **55**, 262 (2015).
[31] K. Onoue and K. S. Breuer, Vortex formation and shedding from a cyber-physical pitching plate, J. Fluid Mech. **793**, 229 (2016).
[32] K. Onoue and K. S. Breuer, A scaling for vortex formation on swept and unswept pitching wings, J. Fluid Mech. **832**, 697 (2017).
[33] Y. Su, M. Miller, S. Mandre, and K. Breuer, Confinement effects on energy harvesting by a heaving and pitching hydrofoil, J. Fluids Struct. **84**, 233 (2019).
[34] A. W. Mackowski and C. H. K. Williamson, Effect of pivot location and passive heave on propulsion from a pitching airfoil, Phys. Rev. Fluids **2**, 013101 (2017).
[35] R. Govardhan and C. H. K. Williamson, Modes of vortex formation and frequency response of a freely vibrating cylinder, J. Fluid Mech. **420**, 85 (2000).
[36] K. Lu, Y. H. Xie, and D. Zhang, Numerical study of large amplitude, nonsinusoidal motion and camber effects on pitching airfoil propulsion, J. Fluids Struct. **36**, 184 (2013).
[37] S. T. Davids, A computational and experimental investigation of a flutter generator, Thesis Dissertation of Naval Postgraduate School, 1999.
[38] F. S. Hover, A. H. Techet, and M. S. Triantafyllou, Forces on oscillating uniform and tapered cylinders in cross flow, J. Fluid Mech. **363**, 97 (1998).
[39] S. Rao, *Mechanical Vibrations*, 4th ed. (Pearson Prentice Hall, Upper Saddle River, NJ, 2004).
[40] J. Eldredge and C. Wang, High-fidelity simulations and low-order modeling of a rapidly pitching plate, in *Proceedings of the 40th Fluid Dynamics Conference and Exhibit, Fluid Dynamics and Co-located Conferences, Chicago, IL* (AIAA, Reston, VA, 2010).
[41] C. Hartloper, M. Kinzel, and D. E. Rival, On the competition between leading-edge and tip-vortex growth for a pitching plate, Exp. Fluids **54**, 1447 (2013).
[42] M. R. Visbal, Unsteady flow structure and loading of a pitching low-aspect-ratio wing, Phys. Rev. Fluids **2**, 024703 (2017).
[43] K. D. Jones, S. Davids, and M. F. Platzer, Oscillating-wing power generation, in *Proceedings of the 3rd ASME/JSME Joint Fluids Engineering Conference* (ASME/JSME, San Francisco, CA, 1999).